Thermal behavior, structure, and dynamics of low-temperature water confined in mesoporous organosilica by differential scanning calorimetry, X-ray diffraction, and quasi-elastic neutron scattering*

Mai Aso[1], Kanae Ito[1], Hiroaki Sugino[1], Koji Yoshida[1], Takeshi Yamada[2], Osamu Yamamuro[2], Shinji Inagaki[3], and Toshio Yamaguchi[1,4,‡]

[1]*Department of Chemistry, Faculty of Science, Fukuoka University, Nanakuma, Jonan-ku, Fukuoka 814-0180, Japan;* [2]*Institute for Solid State Physics, The University of Tokyo, Kashiwanoha, Kashiwa, Chiba 277-0882, Japan;* [3]*Toyota Central R&D Laboratories, Inc., Nagakute, Aichi 480-1192, Japan;* [4]*Advanced Materials Institute, Fukuoka University, Nanakuma, Jonan-ku, Fukuoka 814-0180, Japan*

Abstract: Differential scanning calorimetry (DSC), X-ray diffraction (XRD), and quasi-elastic neutron scattering (QENS) measurements have been made at 200~330 K for capillary-condensed water confined in periodic mesoporous organosilica (PMO) materials with the phenyl groups embedded in silica matrix (Ph-PMO; pore diameter 30 Å). The DSC data showed that the capillary-condensed water in Ph-PMO freezes at 228 K. X-ray radial distribution functions (RDFs) showed that the tetrahedral-like hydrogen-bonded structure of water is distorted in Ph-PMO pores, compared with bulk water; however, with lowering temperature the tetrahedral moiety of water is gradually recovered in the pores. Below the freezing point, cubic ice I_c was formed in the Ph-PMO pores. The QENS data showed that the translational diffusion constant and the residence time and the rotational relaxation time of water molecule in Ph-PMO are comparable with those in bulk. The corresponding activation energies suggested that the more hydrophobic the nature of the wall is, the smaller the activation energy of diffusion and rotation of a water molecule; this implies that water molecules confined in the hydrophobic pores are present in the core of the pores, whereas those in the hydrophilic pores strongly interact with the silanol groups.

Keywords: dynamics; mesoporous materials; neutron scattering; structure; water; X-ray diffraction.

INTRODUCTION

Water in confinement plays an important role in various fields, such as separation in chromatography, catalysts in chemical synthesis, electrical double layers in fuel cells, transport of environmentally haz-

---

ardous materials in clay and soils, and water channels in biological membrane proteins. The structural and dynamical properties of water in confinement at the molecular level are thus essential for understanding the physicochemical properties of confined water and the underlying mechanism of reactions and processes in confined and interfacial systems. For this purpose, a number of studies on thermodynamic, structural, and dynamical properties of water in mesoporous materials have so far been performed by using various techniques, such as calorimetry, Fourier transform-infrared (FT-IR), NMR, X-ray and neutron scattering, etc. Most of the porous materials studied were those of either hydrophilic pores, such as Develosil [1], Vycor [2], MCM-41 [3–7], or hydrophobic ones, such as activated carbon fiber (ACF) [8] and carbon nanotubes (CNTs) [9]. These studies have revealed that water molecules confined in MCM-41 have lower mobility than bulk water, accompanied by distortion of the tetrahedral moieties in the hydrogen-bond network due to the strong hydrogen bonds between interfacial water molecules and the surface silanol groups. On the other hand, the hydrogen-bonded moieties of water confined in hydrophobic pores of ACF is not modified to such an extent as have been observed for water confined in MCM-41 [8]. Thus, the structure and dynamics of water in confinement depend strongly on the nature of the pore wall. Biological systems form pores and interfaces of both hydrophilic and hydrophobic amino acids, and thus the organic–inorganic hybrid porous materials are highly needed. A calorimetric and inelastic neutron scattering (INS) study in this direction has been reported for mesoporous silica whose silanol groups (Si–OH) were modified by hydrophobic octyltriethoxylilane (OTES) [10]. The INS data of water confined in MCM-41-OTES showed vibrational behavior strongly different from bulk water; the data were interpreted by a two-state model, i.e., water molecules with strong hydrogen bonds (O–O distance 2.67 Å) and weak hydrogen bonds (O–O distance of 2.87 Å), compared with those of ice I_h (2.76 Å). Thus, it is of great importance to investigate the structure and properties of water confined in organic–inorganic hybrid mesoporous materials. Recently, a new class of porous materials, periodic mesoporous organosilica (PMO), has been reported [11]. PMO has cylindrical channels of uniform pores in the framework of composite of organic groups and vitreous silica. The organic–inorganic hybrid PMO will offer new possibilities and applications in catalysts, gaseous adsorption, and separation science.

    In this work, the thermal behavior, structure, and dynamic properties of water confined in Ph-PMO at a capillary-condensed state have been investigated at the molecular level over a temperature range of 200–330 K by differential scanning calorimetry (DSC), X-ray diffraction (XRD), and quasi-elastic neutron scattering (QENS) measurements. The dynamics and structure for water in Ph-PMO were compared with those of water confined in MCM-41-C14 (pore diameter 28 Å) [4–7] and in bulk [12]. Finally, the effect of the nature of the pore wall on the structure and dynamics of water is discussed.

EXPERIMENTAL

Preparation of Ph-PMO

Ph-PMO powder was prepared as previously described in [11]. Benzene-bridged organosilane monomer, $(C_2H_5O)_3Si–C_6H_4–Si(OC_2H_5)_3$, [1,4-bis(triethoxysilyl)-benzene, BTEB], was added to an aqueous solution of alkyltrimethylammonium surfactant (3.3 wt %) containing sodium hydroxide, and kept at 368 K for about 20 h. The benzene–silica hybrid material was obtained by collecting the white precipitate (as-made materials), and removing surfactant by solvent extraction. Figure 1 shows the structure model of Ph-PMO. PMO was characterized by XRD, transmission electron microscopy (TEM), and ^{29}Si magic-angle spinning (MAS) NMR. It has a highly ordered mesostructure with well-defined hexagonal, uniform pore-size distribution and high surface area whose interface consists of organic phenyl groups and vitreous silica. The pore diameter, specific surface area, and pore volume were obtained from N_2 adsorption measurements and are summarized in Table 1, together with crystallographic parameters.
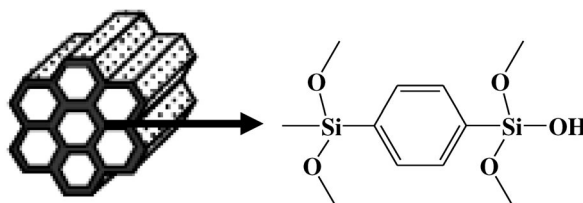
Fig. 1 A structure model of Ph-PMO.

Table 1 Pore diameter D_{BJH} by the Barrett–Joyner–Halenda (BJH) method and D_{DFT} by the density functional theory (DFT) method, pore volume V_p, specific surface area S, lattice value d_{100}, lattice constant a, and thickness between the pores t of Ph-PMO [11]. Parameters d, a, and t were obtained by the relations $d = \lambda/(2\sin\theta)$, $a = d \times 2\sqrt{3}$, and $t = a - D_{DFT}$, where λ is the wavelength of Cu K_α (1.54 Å) and 2θ is the scattering angle of (100) peak (1.92°).

	D_{BJH}/Å	D_{DFT}/Å	V_p/cm^3 g^{-1}	S/m^2 g^{-1}	d_{100}/Å	a/Å	t/Å
Ph-PMO	30	39	0.54	735	46.0	53.1	14

Adsorption/desorption of water

Adsorption and desorption isotherms of water into Ph-PMO pores were measured at 298 K by a free-space method on BELSORP-max (BEL Japan). Before the measurements, the sample was evacuated at 423 K for about 3 h by using a turbo molecular pump. Figure 2 shows the adsorption/desorption isotherms as a function of relative vapor pressure of water. The isotherm is of type V [13]. The figure shows hysteresis between the adsorption and desorption isotherms. Water is adsorbed in Ph-PMO pores in two steps; the first one below P/P_0 ~0.40 corresponds to formation of monolayer water on the pore surface, while the second one above P/P_0 ~0.5 shows capillary condensation of water in the central part of the pores. The sharp jump at the second step reflects very narrow distribution of the pore diameters for the synthesized Ph-PMO.
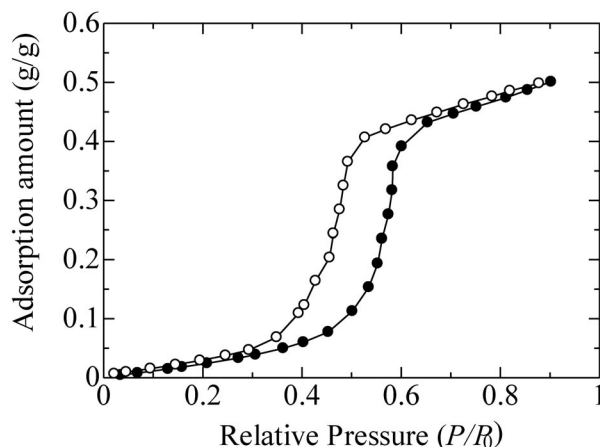
Fig. 2 Adsorption isotherms of water confined in Ph-PMO at 298 K. Adsorption (●) and desorption (○).

Ph-PMO samples filled with water at a required relative vapor pressure of water used for subsequent DSC, XRD, and QENS measurements were prepared on a home-made in situ adsorption apparatus which consists of a vacuum line, a glass flask of water, a turbo molecular pump, a capacitance manometer, and a vacuum gauge. Ph-PMO powder in a cell was placed in a vacuum chamber and evacuated for 1 day with a turbo molecular pump and then exposed to water vapor (relative pressure $P/P_0 =$ 0.90) at 298 K to achieve the capillary condensation of water. This procedure was repeated three times to ensure the surface silanol groups fully chemisorbed with water. After completing adsorption of water into Ph-PMO pores, the samples were contacted with nitrogen gas to an ambient pressure.

DSC measurements

Ph-PMO samples were filled with water under a capillary condensation state at a relative vapor pressure of water $P/P_0 = 0.90$ as described in the previous section. The samples were then contacted with nitrogen gas to an atmospheric pressure and packed in an aluminum cell. DSC measurements were made at a scanning rate of 2 K min^{-1} on DSC6100 (Seiko Instruments, Inc.) that was equipped with a cooling system using liquid nitrogen. The temperature range measured was between 298 and 100 K. The accuracy of temperature was ±1 K.

XRD measurements

Ph-PMO powder was filled into a silica capillary (W. Müller, Inc.) in 2 mm inner diameter and 0.01 mm wall thickness which was connected through a stainless steel flange with a valve through a vacuum line to an in situ adsorption apparatus described previously [5]. The powder sample was dried in vacuum at 298 K for about 24 h, and then gradually exposed to water vapor to $P/P_0 = 0.90$ required for a capillary condensation condition. After completing adsorption of water, the sample was in touch with nitrogen gas to an atmospheric pressure.

X-ray scattering intensities from the capillary condensation of water in Ph-PMO samples were measured at temperatures of 298, 270, 250, 230, 220, and 200 K with a rapid liquid X-ray diffractometer (BRUKER AXS, DIP301) using an imaging plate (IP) as a two-dimensional area detector described elsewhere [14]. The X-rays were generated at a rotary Mo anode (Rigaku, RU-300) operated at 50 kV and 200 mA and then monochromatized with a flat graphite crystal to obtain MoKα radiation (the wavelength $\lambda = 0.7107$ Å). A double-hole type collimator, whose hole-diameter is 0.9 mm, was used to obtain the parallel X-ray beam. The exposure time was 1 h for measurement at each temperature. The camera length is 150 mm. The effective area of IP is 200 × 400 mm, which covers the scattering angle (2θ) of 0–144° and the scattering vector s ($= 4\pi\lambda^{-1}\sin\theta$) of 0–16.0 Å^{-1}. This wide range of scattering vector enables us to derive highly resolved radial distribution functions (RDFs) by reducing the termination error in Fourier transformation of structure functions mentioned later. After the irradiation, information on scattered intensities on IP was obtained by stimulating with a He–Ne laser beam ($\lambda = 632.8$ nm) and measuring the luminescence ($\lambda = 390$ nm) on a photomultiplier tube.

Cooling of the sample was carried out by using a specially designed cryostat (Rigaku, Inc.) of blowing cold N$_2$ gas from liquid N$_2$ on the capillary. The temperature of the sample was measured by a copper-constantan thermocouple and controlled within ±1 K by adjusting the blow rate of N$_2$ gas.

After X-ray measurements of capillary-condensed water sample, the valve of the flange was opened to desorb water from Ph-PMO powder to prepare the dry sample with a turbo molecular pump. The X-ray scattering intensities of the dry Ph-PMO sample were then measured at the same temperatures as measured for the water-doped samples.

The X-ray scattering intensities of a water-adsorbed sample (wet) on Ph-PMO, $I_{wet}(s)$, can be represented as

$$I_{wet}(s) = I_{water}(s) + I_{water-Ph-PMO}(s) + I_{Ph-PMO}(s) + I_{cell}(s) \tag{1}$$

where $I_{water}(s)$ is the intensity of water adsorbed in Ph-PMO, $I_{water-Ph-PMO}(s)$ is that of interactions between water molecules and silica walls, $I_{Ph-PMO}(s)$ is that of Ph-PMO itself, and $I_{cell}(s)$ is that of the cell alone.

On the other hand, the X-ray intensities of a dry sample, $I_{dry}(s)$, can be written as

$$I_{dry}(s) = I_{Ph-PMO}(s) + I_{cell}(s) \tag{2}$$

Therefore, the X-ray scattering intensities related to the adsorbed water in the pores are obtained by subtracting eq. 2 from eq. 1 as

$$I_{coh}(s) = I_{wet}(s) - I_{dry}(s) = I_{water}(s) + I_{water-Ph-PMO}(s) \tag{3}$$

The experimental intensities, I_{coh}, were corrected for multiple scattering and Compton scattering as described elsewhere [14]. The structure function, $i(s)$, is given by

$$i(s) = K[I_{water}(s) + I_{water-Ph-PMO}(s)] - \sum_i x_i f_i^2(s) \tag{4}$$

where K represents a factor to normalize the experimental intensities to absolute units in a usual manner [15–17], x_i is the number of atom i in a stoichiometric volume, $f_i(s)$ is the atomic scattering factor of atom i corrected for the anomalous dispersion.

The RDF, $D(r)$, was calculated by means of FT as

$$D(r) = 4\pi r^2 \rho_0 + 2r\pi^{-1} \int_0^{s_{max}} si(s)M(s)\sin(rs)ds \tag{5}$$

Here, $\rho_0 (= [\Sigma x_i f_i(0)]^2/V$ stands for the average scattering density of a sample solution in the stoichiometric volume V, and s_{max} is the maximum s value attained in the measurements ($s_{max} = 16$ Å^{-1}). A modification function $M(s)$ of the form $[\Sigma x_i f_i(0)^2/\Sigma x_i f_i(s)^2] \exp(-0.01 s^2)$ was used.

A comparison between the experimental structure function and the theoretical one based on a model was made by a least-squares refinement procedure of minimizing an error squares sum over a selected s region from s_{min} to s_{max}

$$U = \sum_{s_{min}}^{s_{max}} s^2\{i(s)_{exp} - i(s)_{calc}\}^2 \tag{6}$$

The theoretical intensities, $i(s)_{calc}$, were obtained by

$$i(s)_{calc} = \sum_i \sum_j x_i x_j n_{ij} f_i(s) f_j(s) \sin(r_{ij}s)(r_{ij}s)^{-1} \exp(-b_{ij}s^2) \tag{7}$$

This term is related to the short-range interactions characterized by the interatomic distance r_{ij}, the temperature factor b_{ij} and the number of interactions n_{ij} for atom pair i–j. All treatments of the XRD data were carried out with the program KURVLR [18].

QENS measurements

A sample of water adsorbed in Ph-PMO pores at a capillary condensation state was prepared at $P/P_0 = 0.90$ as described in the previous sections. The powder samples were inserted into a double-cylinder aluminum cell, which consists of an inner cylinder of 14.0 mm outer diameter, 0.25 mm thickness, and 45 mm height and an outer cylinder of 18.0 mm inner diameter, 0.25 mm thickness, and 50 mm height. The thickness of the sample was 1 mm, which gave transmission of neutrons of more than 90 %.

The neutron scattering measurements were carried out with a time-of-flight-type spectrometer AGNES (angle-focusing neutron spectrometer) owned by the Institute for Solid State Physics, The University of Tokyo, and installed at the JRR-3 reactor of Japan Atomic Energy Research Institute. The

details of the spectrometer have been described elsewhere [19]. The wavelength λ of incident neutrons was 4.22 Å, the scattering vector Q ($= 4\pi\lambda^{-1}\sin\theta$, 2θ is the scattering angle) covered was 0.2~2.7 Å^{-1}, the energy transfer ω varied within –2~+2 meV. The energy resolution was 120 μeV which was estimated from the data measured at 150 K, where the confined water was regarded as frozen at the present time scale. The measurements were performed at 270, 285, 300, 315, and 330 K.

## RESULTS AND DISCUSSION

DSC measurements

Figure 3 shows the DSC curve of water in Ph-PMO at capillary condensation state. The data show an exothermic peak at 228 K, which is attributed to the freezing of water, and an endothermic peak at 223 K due to melting of ice. On the other hand, the DSC curves of water in MCM-41 C14 at capillary condensation state showed an exothermic peak at 225 K and an endothermic peak at 221 K [7]. Confined water tends to crystallize at temperatures higher by ~2 K in Ph-PMO pores than in MCM-41 C14 pores when hydrophobic phenyl groups are embedded in the silica wall.
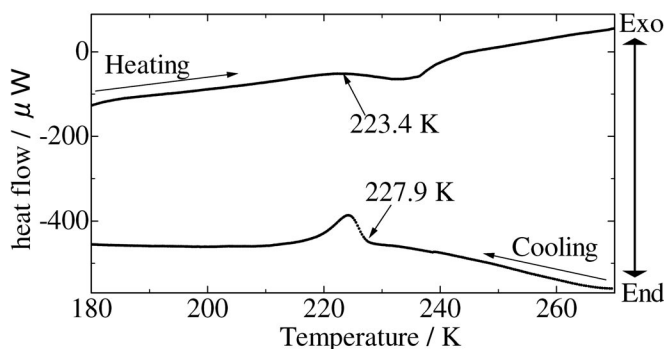

Fig. 3 DSC curve of water in Ph-PMO at $P/P_0 = 0.90$. The scanning speed was 2 K/min.

XRD measurements

Figure 4 shows the s-weighted structure functions of the capillary-condensed water in Ph-PMO pores, together with that of bulk water at 298 K for comparison. At the temperatures below 230 K Bragg peaks appeared at $s = 1.7$ and 2.7 Å^{-1} and were evolved with lowering temperature. These peaks were due to the formation of ice as expected from the DSC data (freezing point 228 K) in the previous section and in Fig. 3. Figure 5 shows the X-ray scattering intensities as a function of the Bragg angle θ for water in Ph-PMO at 200 K. The Bragg peaks ascribed to ice are numbered, and the corresponding lattice space values d were calculated and summarized in Table 2. From a comparison of the present values with the literature data for bulk hexagonal ice I_h and cubic ice I_c [1], the ice formed in Ph-PMO was assigned to cubic ice I_c. Cubic ice was also found in other confined systems, such as Spherisorb S20W [19] and Develosil 100 [1].
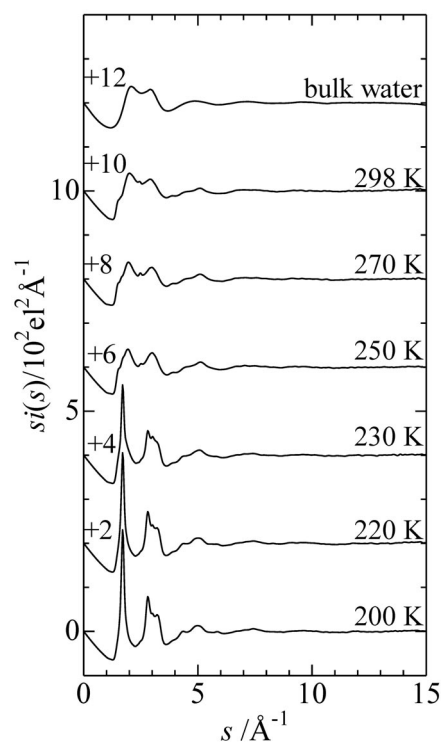
Fig. 4 The *s*-weighted experimental structure functions, *i*(*s*), for water confined in Ph-PMO at different temperatures, together with that of bulk at 298 K for comparison.
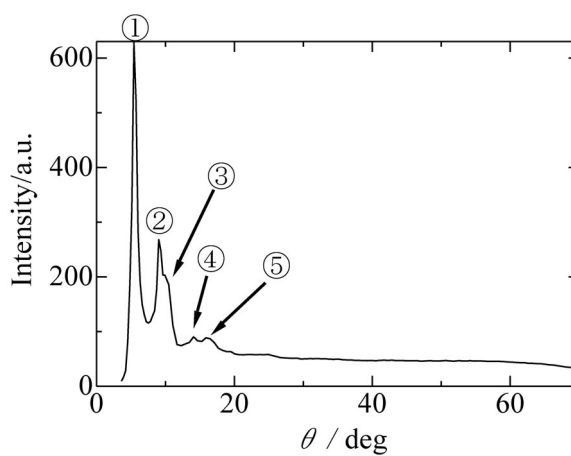

Fig. 5 The XRD pattern of water confined in Ph-PMO at 200 K. The numbers represent Bragg peaks due to the formation of cubic ice.

Table 2 The lattice value d (Å) of ice formed in Ph-PMO, together with those of ice I_h and I_c for bulk water [1]. The figures in parentheses correspond to the Bragg peaks numbered in Fig. 5.

H$_2$O in Ph-PMO	I_c	I_h
(1) 3.69	3.68	3.90
(2) 2.24	2.25	3.66
(3) 1.95	1.92	3.40
	1.59	2.67
(4) 1.46	1.46	2.25
(5) 1.30	1.30	2.07

Figure 6 shows the RDFs obtained by FT of the structure functions in Fig. 4. The hydrogen-bonded structure of bulk water is characterized by the distinct peak at 2.85 Å due to the first-neighbor water–water interactions, the broad double peaks centered at 4.1 and 4.6 Å due to the second neighbors, and the broad peak centered at 6.8 Å ascribed to the third-neighbor interactions. The RDF of the Ph-PMO capillary-condensed water at 298 K has a similar pattern at 2.85 Å to that of bulk water. It
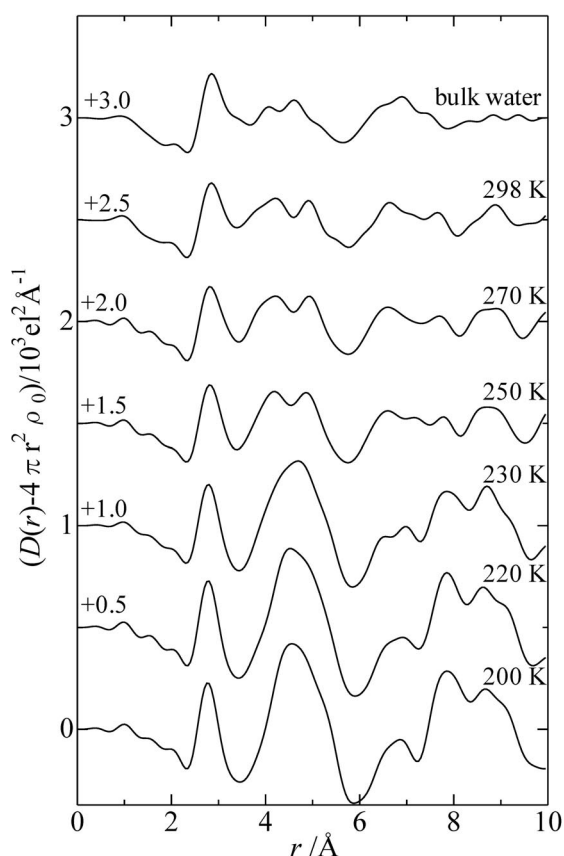
Fig. 6 The RDFs in the form of $D(r) - 4\pi r^2 \rho_0$ for water confined in Ph-PMO at different temperatures, together with that of bulk at 298 K for comparison.

should be noted here that the first peak also includes the OH–H_2O interactions between the silanol groups and water molecules hydrogen-bonded to them. The second peaks are observed at 4.2 and 4.9 Å for water in Ph-PMO, both longer than those for bulk water. In addition, a shoulder is also seen at 3.8 Å. The latter shoulder has been assigned to the water–silanol group interactions (Si–H_2O) [5]. The third peaks are seen at a distance similar to that of bulk water, but accompanied by additional long-range interactions at 7~10 Å. In the case of capillary-condensed water confined in MCM-41-C14 [5], the first and second peaks were observed at 2.84, 4.1, and 4.8 Å, respectively. A comparison among these results suggests that the first-neighbor water–water and/or water–silanol OH interactions fall in a similar region within experimental uncertainties among the three systems; however, the second-neighbor water–water interactions are substantially distorted for confined water, in particular, for Ph-PMO, as the peak position of 4.9 Å much longer than 4. 65 Å (= 2.85 Å × $\sqrt{(8/3)}$) expected for tetrahedrally arranged water molecules in bulk water. These findings show that the tetrahedral ordering of confined water is very distorted, compared with bulk water, due probably to the confinement and interfacial effects.

When temperature was lowered, the double peak due to the second-neighbor interactions at 4.1 and 4.9 were gradually developed. At the temperatures below 230 K, the double peaks were merged into a predominant single peak at 4.6 Å. These results show that the tetrahedral-like structure of water is partially recovered for confined water due to development of hydrogen bonds between water molecules and also the formation of cubic ice below 230 K. At temperatures below 230 K, the third-neighbor interactions are characterized by an enhanced broad peak in the range of 7.5–9.5 Å, again due to ice formation.

To analyze the interactions quantitatively, the model fitting was applied to the structure functions. All calculations were performed with the program NLPLSQ [21]. In subsequent analysis of the X-ray data, all the interactions discussed above were taken into account. The initial values of distances r_{ij}, coordination numbers n_{ij}, and temperature factors b_{ij} of each interaction were estimated by a trial-and-error analysis in *r*-space where the observed RDFs were compared with theoretical peak shapes calculated with eqs. 5 and 7. The distance, coordination number, and temperature factor were all allowed to vary in the first stage of the fitting procedure. However, since the temperature factor strongly correlates with the coordination number, as seen in eq. 7, the temperature factors were fixed to the values obtained at 298 K in subsequent fittings, so that the change in coordination number with temperature was figured out. The parameter values of the optimal models are summarized in Table 3. Theoretical functions calculated by using the values in Table 3 were plotted in Figs. 7 and 8. The agreement between the experiments and the models is fairly good. The disagreement between the observed and calculated values in the low *s*-region below 3 Å^{-1} in Fig. 7 is caused by the long-range interactions above ~5 Å not taken into account in the model as shown in Fig. 8. The temperature dependences of the coordination number of waters in the first- and second-neighbor interactions are illustrated in Fig. 9. The coordination number of water molecules at the distance of 2.8 Å increased with decreasing temperature. At the same time, the coordination number of water molecules at 4.8 Å also increased. Since both interactions are ascribed to those in the hydrogen-bonded network of water, the results show that the hydrogen-bonded water structure is gradually enhanced in the pores with decreasing temperature. The coordination number of the non-hydrogen-bonded water molecules at the distance of 3.1 Å decreased with cooling of both capillary-condensed samples. This result suggests that the non-hydrogen-bonded water molecules are stabilized in the enhanced tetrahedral-like water structure at the low temperatures.

Table 3 Interatomic distance r, temperature factor b, and the number of interactions n of models obtained by the least-squares fits in Fig. 7 for water in Ph-PMO, together with those for water confined in MCM-41 C14 [5]. The estimated standard deviations in r and n are ±0.01 Å and ±0.2, respectively.

|		Ph-PMO	MCM-41 C14	Ph-PMO	MCM-41 C14	Ph-PMO	MCM-41 C14
		298 K		270 K		250 K	
O–O 1st	r/Å	2.76	2.81	2.80	2.79	2.77	2.78
	b/Å²	0.010*	0.010*	0.010*	0.010*	0.010*	0.010*
	n	1.4	2.9	1.7	3.4	1.6	3.4
O–O 2nd	r/Å	4.16	4.35	4.16	4.37	4.14	4.39
	b/Å²	0.020*	0.020*	0.020*	0.020*	0.020*	0.020*
	n	2.5	2.8	2.5	3.7	2.6	4.3
O–O 2nd	r/Å	4.86	4.94	4.85	4.90	4.81	4.90
	b/Å²	0.030*	0.023*	0.030*	0.023*	0.030*	0.023*
	n	2.3	2.4	2.4	3.4	2.9	3.6
O–O non H-bond	r/Å	3.10	3.34	3.18	3.35	3.13	3.33
	b/Å²	0.010*	0.012*	0.010*	0.012*	0.009*	0.012*
	n	1.2	1.9	0.6	1.3	0.8	1.5
O–Si (silanol)	r/Å	3.62	3.92	3.65	3.90	3.65	3.90
	b/Å²	0.020*	0.015*	0.020*	0.015*	0.020*	0.015*
	n	0.86	1.4	0.74	1.3	0.7	1.2

*Fixed during the calculations.
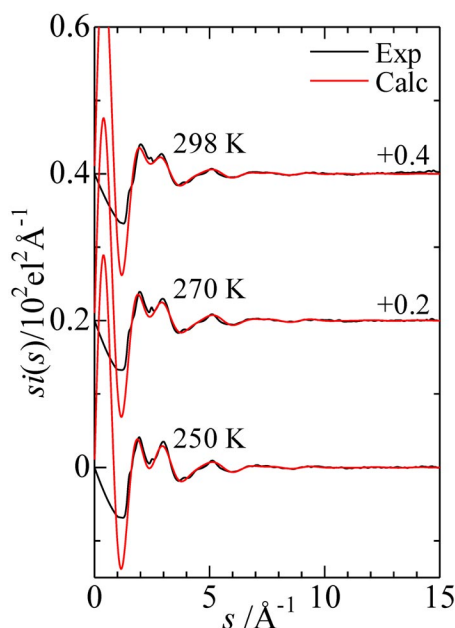
Fig. 7 The results of least-squares fits applied to the s-weighted structure functions over the s-range of 3–12 Å⁻¹. The black lines show the experimental values, the red lines the calculated values by using the model parameters in Table 3. (This figure is in colour only in the electronic version.)
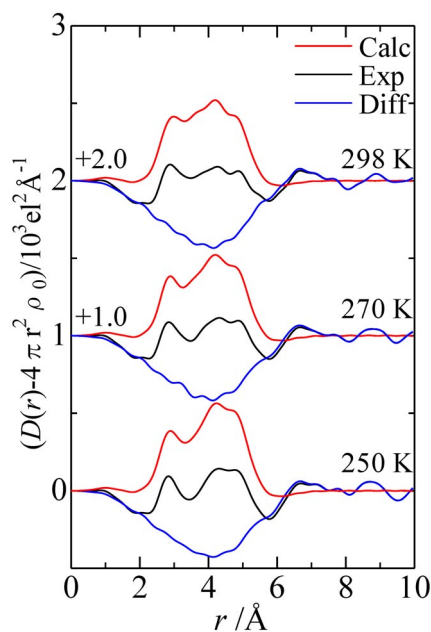
Fig. 8 The results of least-squares fits obtained by the FT of the values in Fig. 7. The black lines show the experimental values, the red lines the calculated values by using the model parameters in Table 3, and the blue lines their difference. (This figure is in colour only in the electronic version.)
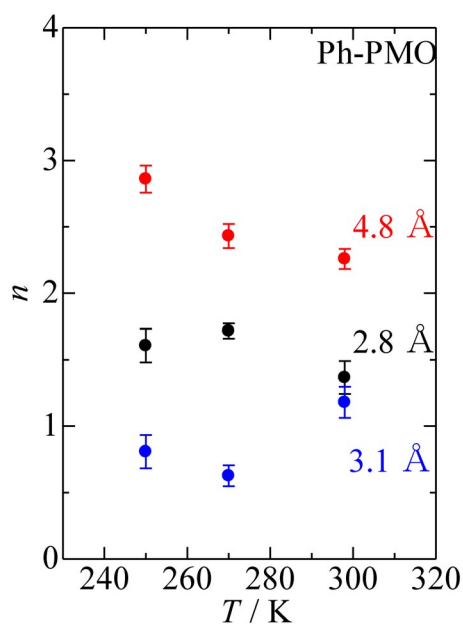
Fig. 9 The coordination number of water molecules at 2.8 and 4.8 Å related to the hydrogen-bonded interactions and 3.1 Å for non-hydrogen-bonded interactions. (This figure is in colour only in the electronic version.)

QENS measurements

Figure 10 shows the temperature dependence of QENS spectra of water confined in Ph-PMO at $Q = 1.6\ \text{Å}^{-1}$. The individual spectra are shifted for clarity. The values measured at 150 K were used for instrument resolution since the motion of water molecules can be regarded as frozen on the time scale of this spectrometer. With lowering temperature, the peak width is gradually decreased, showing that the motion of the water molecule is slowed down with lowering temperature.
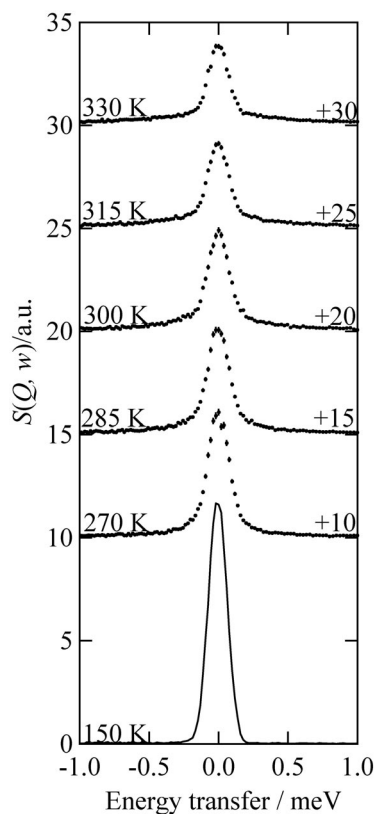
Fig. 10 The temperature dependence of the QENS spectra of water confined in Ph-PMO at $P/P_0 = 0.90$ and at $Q = 1.6\ \text{Å}^{-1}$.

The QENS spectra were analyzed by a model of both translational and rotational diffusions of water molecules [4,12,22], from which the self-diffusion coefficient D and the residence time τ_0 of translational diffusion, and the relaxation time τ_1 of rotational diffusion were derived. The scattering law $S(Q, \omega)$ of the water-filled sample, which consists of contributions from water and Ph-PMO, can be expressed by relation 8.

$$S(Q,\omega) = \left\{ \delta(\omega) + \exp\left(-\frac{Q^2 \langle u \rangle^2}{3} \right) L_{\text{Trans}}(Q,\omega) \otimes L_{\text{Rot}}(Q,\omega) \right\} \otimes R(Q,\omega) + BG \tag{8}$$

$<u^2>$ is the mean-square vibrational amplitude of water molecules. $\delta(\omega)$ is a δ function and corresponds to the elastic component. $\otimes$ signifies a convolution in ω. $L_{\text{trans}}(Q, \omega)$ and $L_{\text{rot}}(Q, \omega)$ are contributions

from translational and rotational diffusions of the capillary-condensed water molecules, respectively. BG is the background and $R(Q, \omega)$ is the resolution function. $L_{\text{trans}}(Q, \omega)$ is expressed by eq. 9.

$$L_{\text{trans}}(Q,\omega) = \frac{1}{\pi}\frac{\Gamma(Q)}{\left[\omega^2 + \Gamma(Q)^2\right]} \tag{9}$$

Here, $\Gamma(Q)$ is defined as eq. 10.

$$\Gamma(Q) = \frac{D_{\text{trans}}Q^2}{1 + D_{\text{trans}}Q^2\tau_0} \tag{10}$$

$L_{\text{rot}}(Q, \omega)$ is calculated by eq. 11.

$$L_{\text{rot}}(Q,\omega) = j_0^2(Qa)\delta(\omega) + \frac{1}{\pi}\sum_{l=1}^{\infty}(2l+1)j_l^2(Qa)\frac{l(l+1)D_{\text{rot}}}{\omega^2 + \left[l(l+1)D_{\text{rot}}\right]^2}, \tag{11}$$

where $j_l(Qa)$ are spherical Bessel functions. a stands for the radius of rotation (0.98 Å, the O–H distance of water molecule). D_{rot} is the diffusion coefficient of rotation. The relaxation time τ_1 of rotational diffusion is related to D_{rot} by eq. 12.

$$\tau_{\text{rot}} = \frac{1}{6D_{\text{rot}}} \tag{12}$$

Figure 11 shows the typical fitting result by a model using eq. 8 applied to the QENS data of water confined in Ph-PMO at $P/P_0 = 0.90$, at $Q = 1.6$ Å^{-1} and at 330 K. Figures 12–14 show the Arrhenius plots of the self-diffusion coefficient D_{trans} and the residence time τ_0 of translational diffusion and the relaxation time τ_{rot} of rotational diffusion for water confined in Ph-PMO. Those of bulk water [12] and water confined in MCM-41 C14 [4,6] are also plotted in both figures for comparison.
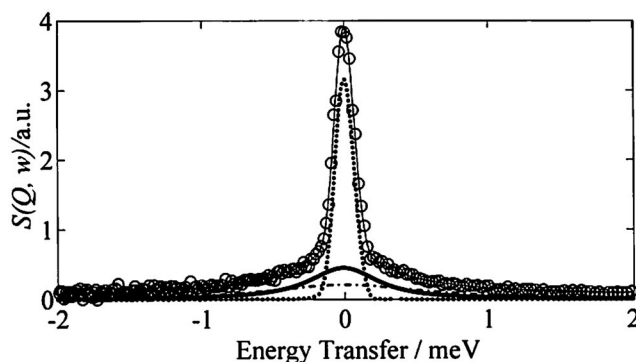

Fig. 11 The fitting result of the Teixeira method [22] applied to the QENS data of water confined in Ph-PMO at $P/P_0 = 0.90$, at $Q = 1.6$ Å^{-1} and at 330 K. Circles denote the experimental data, dots the elastic component, thick solid line quasielastic component (translation), line and dot the quasielastic component (rotation), and thin solid line their sum.
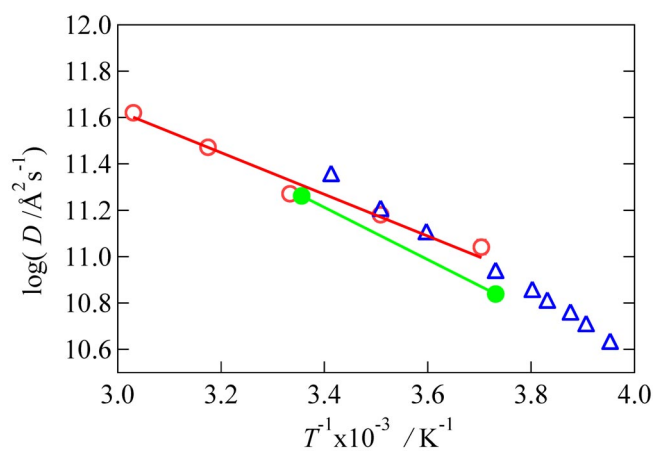
Fig. 12 The Arrhenius plot of diffusion coefficient D of translational diffusion for water confined in Ph-PMO (○) and in MCM-41 C14 (●) [4,6], and in bulk (△) [12].
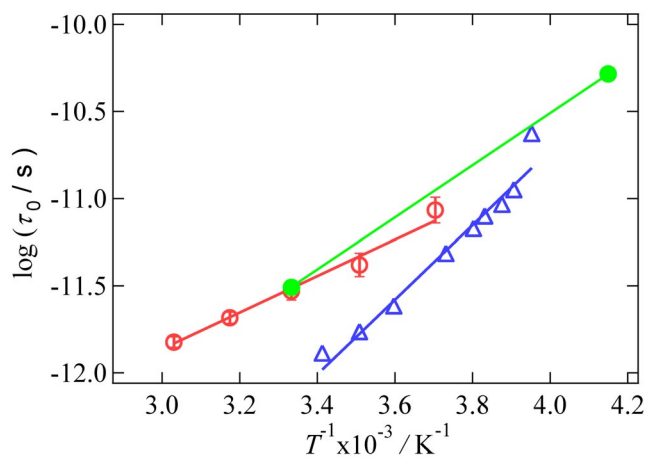
Fig. 13 The Arrhenius plot of residence time τ_0 of translational diffusion for water confined in Ph-PMO (○) and in MCM-41 C14 (●) [4,6], and in bulk (△) [12].
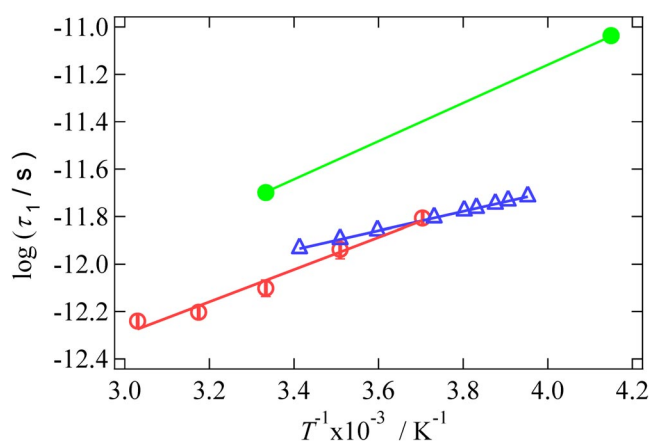
Fig. 14 The Arrhenius plot of relaxation time τ_1 of rotational diffusion for water confined in Ph-PMO ($\bigcirc$) and in MCM-41 C14 ($\bullet$) [4,6], and in bulk ($\triangle$) [12].

The self-diffusion coefficient of confined water decreased and resides for a longer time at a given place, i.e., the translational diffusion of confined water is slower than that of bulk water due to the confinement and interfacial effects. When the hydrophobicity of the confined wall increases, the values of self-diffusion coefficient of the water molecule are larger for Ph-PMO pores than those for MCM-41 C14 pores. The relaxation time of rotational diffusion of the water molecule confined in Ph-PMO is shorter than those in MCM-41 C14 and bulk water, i.e., the rotational diffusion of a water molecule is less hindered in Ph-PMO pores than in MCM-41 C14 pores since the interfacial water molecules in Ph-PMO are hydrogen-bonded to the silanol groups to a lesser extent than those in MCM-41 C14 pores.

The activation energy E_a (kJ/mol) obtained from the Arrhenius plots are summarized in Table 4. Confined water in Ph-PMO diffuses and rotates with a smaller E_a than in MCM-41 C14 due to the effect of interfacial interaction. When the hydrophobicity of the confined wall increases, confined water diffuses and rotates with smaller energy. It is most likely that water molecules confined in the hydrophobic interface will tend to assemble in the center part of the pores, while water molecules confined in the hydrophilic interface strongly interact with the silanol groups.

Table 4 The activation energy E_a obtained from the Arrhenius plots of translational diffusion coefficients D, residence time τ_0, and rotational correlation time τ_{rot} for water molecules confined in Ph-PMO.

	$E_a(D)$/kJ mol^{-1}	$E_a(\tau_0)$/kJ mol^{-1}	$E_a(\tau_{rot})$/kJ mol^{-1}	Refs.
MCM-41 C14	21.6	28.7	15.6	4
Ph-PMO	17.2 ± 0.9	20.0 ± 1.8	13.0 ± 1.0	This work
Bulk	17.9 ± 0.9	25.9 ± 1.8	13.5 ± 0.8	12

CONCLUSION

The thermal properties, structure, and dynamics of capillary-condensed water confined in Ph-PMO porous materials with phenyl groups embedded in silica matrix (pore diameter 30 Å) were characterized by DSC, XRD, and QENS measurements. The information obtained for water in Ph-PMO was compared with that of water in non-modified MCM-41 (pore diameter 28 Å) from a standpoint of hydrophilic and hydrophobic properties of pore walls. The DSC data showed an exothermic peak at 228 K attributed to the freezing of water and an endothermic peak at 235 K due to melting of ice. From

an analysis of XRD data in terms of the RDFs, it was found that the hydrogen-bonded network of water is distorted in Ph-PMO pores, compared with that in bulk water, and that confined water in Ph-PMO crystallizes as cubic ice I_c below the freezing point. The model fitting showed that the coordination number of water molecules at 2.8 and 4.8 Å increases, whereas the amount of non-hydrogen-bonded water molecules at 3.1 Å decreases with lowering temperature. It proved the evolution of hydrogen-bonded structure in the adsorbed water with decreasing temperature. The QENS data were analyzed by the Teixeira method [22] and obtained the diffusion coefficient and the relaxation time of translational and rotation motions of confined water molecules, together with their E_as. It was found that water molecules confined in Ph-PMO diffuse and rotate with a smaller E_a than in MCM-41 C14 because of the effect of interfacial interaction. From a comparison of the corresponding data of water confined in MCM-41, it was found that the more hydrophobic the pore wall becomes, the smaller the E_a the confined water molecules diffuse and rotate with.

ACKNOWLEDGMENTS

REFERENCES

1. T. Takamuku, M. Yamaguchi, H. Wakita, Y. Masuda, T. Yamaguchi. *J. Phys. Chem. B* **101**, 5730 (1997).
2. M.-C. Bellissent-Funel, S. Longeville, J.-M. Zanotti, S.-H. Chen. *Phys. Rev. Lett*. **85**, 3644 (2000).
3. J. S. Beck, J. C. Vartulli, W. J. Roth, M. E. Leonovicz, C. T. Kresger, K. D. Schmitt, C. T.-W. Chu, D. H. Olson, E. W. Sheppard, S. B. McCullen, J. B. Higgins, J. L. Schlenker. *J. Am. Chem. Soc.* **114**, 10834 (1992).
4. S. Takahara, M. Nakano, S. Kittaka, Y. Kuroda, T. Mori, H. Hamano, T. Yamaguchi. *J. Phys. Chem. B* **103**, 5814 (1999).
5. P. Smirnov, T. Yamaguchi, S. Kittaka, S. Takahara, Y. Kuroda. *J. Phys. Chem. B* **104**, 5498 (2000).
6. S. Takahara, N. Sumiyama, S. Kittaka, T. Yamaguchi, M.-C. Bellissent-Funel. *J. Phys. Chem. B* **109**, 1231 (2005).
7. K. Yoshida, T. Yamaguchi, S. Kittaka, M.-C. Bellissent-Funel, P. Fouquet. *J. Chem. Phys*. **129**, 054702 (2008).
8. T. Yamaguchi, H. Hashi, S. Kittaka. *J. Mol. Liq*. **129**, 57 (2006).
9. Y. Maniwa, H. Kataura, M. Abe, S. Suzuki, Y. Achiba, H. Kira, K. Matsuda. *J. Phys. Soc. Jpn.* **71**, 2863 (2002).
10. E. Levy, A. I. Kolesnikov, J. Li, Y. Mastai. *Surf. Sci*. **603**, 71 (2009).
11. S. Inagaki, S. Guan, T. Ohsuna, O. Terasaki. *Nature* **416**, 304 (2002).
12. T. Yamada, R. Yonamine, T. Yamada, H. Kitagawa, M. Tyagi, M. Nagao, O. Yamamuro. *J. Phys. Chem. B* **115**, 13563 (2011).
13. S. Brunauer, L. S. Deming, W. E. Deming, E. Teller. *J. Am. Chem. Soc.* **62**, 1723 (1940).
14. K. Yamanaka, T. Yamaguchi, H. Wakita. *J. Chem. Phys*. **101**, 9830 (1994).
15. K. Furukawa. *Rep. Prog. Phys*. **25**, 395 (1973).
16. J. Krogh-Moe. *Acta Crystallogr*. **9**, 951 (1956).
17. N. Norman. *Acta Crystallogr*. **10**, 370 (1957).
18. G. Johansson, M. Sandström. *Chem. Scr*. **4**, 195 (1973).

19. T. Kajitani, K. Shibata, S. Ikeda, M. Kohgi, H. Yoshizawa, K. Nemoto, K. Suzuki. *Physica B* **213–214**, 872 (1995).
20. J. C. Dore, M. Dunn, P. Chieux. *J. Phys. Coll. C1* Suppl. 3, **48**, 457 (1987).
21. T. Yamaguchi. Doctoral Thesis, Tokyo Institute of Technology (1978).
22. J. Teixeira, M.-C. Bellissent-Funel, S. H. Chen, A. J. Dianoux. *Phys. Rev. A* **31**, 1913 (1985).